IFASD 2015
International Forum on Aeroelasticity and Structural Dynamics
June 28 — July 02, 2015 ▲ Saint Petersburg, Russia

LIMIT-CYLCLE-OSCILLATION SIMULATIONS OF AEROSTABIL WINDTUNNEL EXPERIMENTS

Bernd Stickan[1], Johannes Dillinger[1], and Jens Nitzsche[1]
[1]DLR - Institute of Aeroelasticity
Bunsenstraße 10, 37073 Göttingen
Bernd.Stickan@dlr.de
Johannes.Dillinger@dlr.de
Jens.Nitzsche@dlr.de

Keywords: Aerostabil, Limit-Cycle-Oscillations, CFD-CSM-Interaction, TAU, Unsteady Aerodynamics, Nonlinear Structure

Abstract

A series of windtunnel experiments conducted in the Transonic Windtunnel Göttingen (TWG) allowed the observation of Limit-Cycle-Oscillations of a backwards-swept, clean wing for a certain transonic parameter range. As additional feature the Aerostabil wing model shows cambering effects, which have a strong influence on transonic aerodynamics.

This paper is following [13] and in more detail [14]. In these reports first simulation results employing computation fluid dynamics (CFD) and detailed computational structural mechanics (CSM) of the AEROSTABIL experiment have been shown. But the structural modelling has been limited to one dynamic degree of freedom. In this paper the structural representation is expanded to 2 dynamic degrees of freedom which allow a better agreement to the experimental data. The LCO mechanism is hereby confirmed: Strong shock movement leads to aerodynamic nonlinearities.

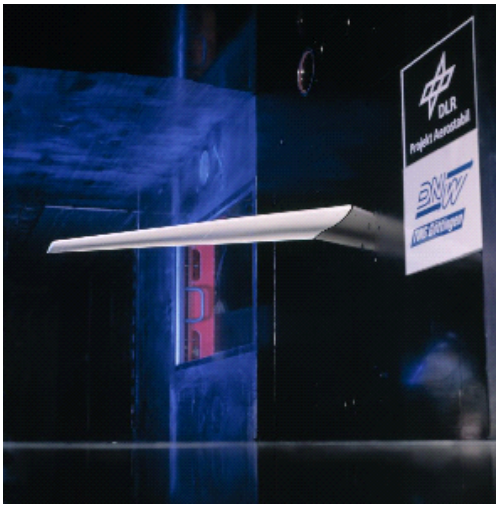

Figure 1: Aerostabil model inside the TWG

1 INTRODUCTION

In 2001/2002 measurements have been performed with the so-called Aerostabil wing (model B). The aim of the experiments was the investigation of the static and dynamic behaviour of an elastic wing under transonic aerodynamic loads [3].

The Aerostabil wing has 0.601m span,

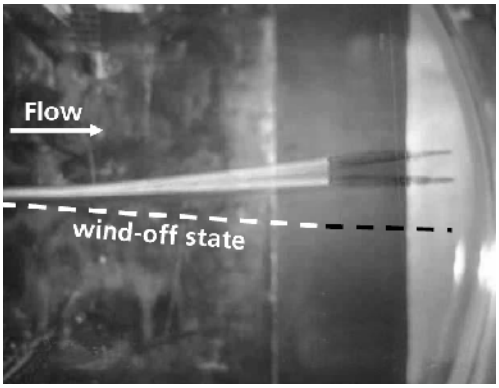

Figure 2: Aerostabil wing in LCO state

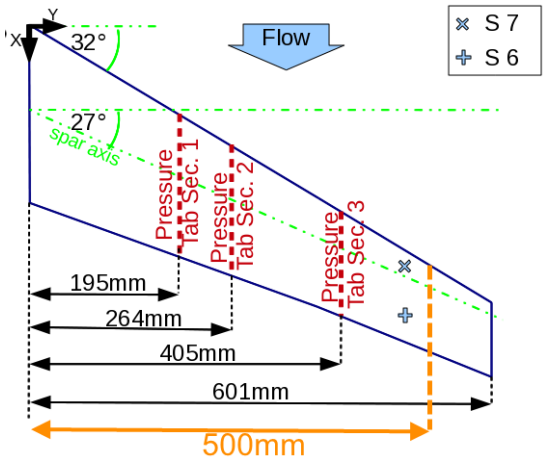

Figure 3: Aerostabil wing sketch:
3 pressure tab sections:
- upper side: 18/18/15 kulites
- lower side: 16/14/12 kulites
acceleration sensors S6 and S7
(Cut at $y = 0.5m$ used as simulation analysis section only)

an aspect ratio of 3.68, 32° leading-edge sweepback angle and is composed of supercritical airfoils. As materials glass and carbon fibre composites have been used. The measurements in the TWG have been performed for *Mach*-numbers between 0.5 and 0.89 and *Reynolds*-numbers from $0.7 \cdot 10^6$ up to $2.2 \cdot 10^6$. The LCOs were measured for *Mach*-numbers at about $Ma = 0.87$ and angles of attack of 2.7°. The frequencies of the LCOs are approximately 50Hz.

The basic equipment of the model can be observed in Figure 3. The sketch shows the three pressure measurement sections and additionally two acceleration sensors which are used in the comparisons between simulation and experiment in the sections below. Additionally a cut at $y = 0.5m$ is plotted. This cut does not have any pressure measurement devices, but is used in the upcoming studies as observation cut of simulation results. This is necessary since for the expected simulation result the most important part is the outer-wing area.

After introducing the used methods for the static and dynamic investigations

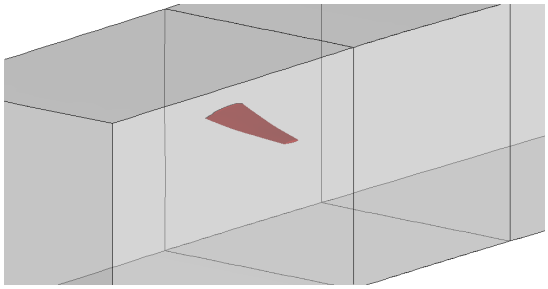

Figure 4: CFD-model including windtunnel walls

including the classical p-k-method for stability computations and time-domain LCO simulations, it is reminded about the structural features of the windtunnel model and the steady flow conditions in LCO vicinity in Section 3. Afterwards the results of a two dynamic two degree-of-freedom system are show. Section 4 shows the flutter result and their comparison the measured stability ranges, while the Section 5 presents some limit-cycle-oscillation results.

2 NUMERICAL METHODS

This section presents the employed numerical methods.

The static CFD-CSM computations are either performed with a linear or a non-linear structural model. While the linear model is used in generalized coordinates (with a sufficient number of modes), the non-linear computations are performed by calling NASTRAN with the SOL 400 solution sequence. This solution covers structural nonlinearities by stepwise updating the structural stiffness matrix. The method included differential stiffness and geometric non-linear effects, see [9].

The unsteady computations are always performed with a generalized structural model. These time-domain simulations are performed with a Newmark time integration, [1, p. 322], while the frequency domain equations are solved with the p-k-method shown in [6]. The aerodynamics is in both cases computed with CFD. For

the time-domain computations the structural solver and the CFD solver are alternated stepwise in a weak-coupled procedure, while for the frequency-domain analysis the Pulse-method as seen in [11] is applied.

As aerodynamic CFD solver the DLR TAU-code is applied to solve the steady and the unsteady Reynolds Averaged Navier Stokes (RANS) equations [5]. This finite-volume code employs the LUSGS-scheme for steady and the 2^{nd} order dual time-stepping for unsteady computations, see [4, 7]. For the presented simulations central flux and scalar dissipation are used. As turbulence model the Menter SST model is applied, see [8].

The coupling of structural and aerodynamic model is performed with radial-basis function interpolation, coupling the surface of the structural model to the surface of the CFD-mesh, see [2]. The created coupling matrix guarantees virtual-work conservation for the time-domain simulations and can also be used for the eigenmode-interpolation necessary for the frequency-domain simulations.

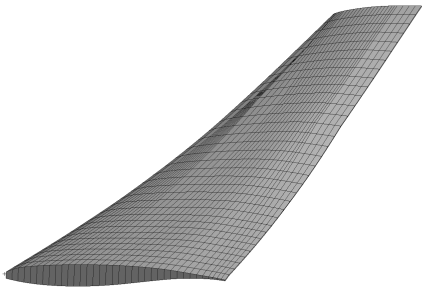

Figure 5: Shell model, deformed in first bending mode

The method to deform the CFD-mesh is also using radial basis function interpolation. To optimize the performance only a limited number of base-points are used for the interpolation. Therefore in a second deformation step the surface interpolation error is eliminated with a nearest-surface-neighbour correction method as proposed in [10].

3 REMINDER: STRUCTURAL FEATURES AND STEADY FLOW CONDITIONS

As already presented in [12] the Aerostabil wing airfoils camber under load in an order of magnitude which cannot be neglected. Figure 6 shows a comparison of aerodynamic results with and without airfoil deformation. It shows clearly the importance of detailed structural model to cover the steady aerodynamics. Therefore a detailed structural model is the key for CFD-CSM simulations. Figure 5 shows the structural model in the first bending mode.

Self-evident the detailed structural modelling is also mandatory for the flow settings at LCO conditions. Figure 7, which has already been shown in [13], should give an overview about the flow features at these conditions. The pressure plots indicate a two-shock system, while the skin-friction lines show a strong separation downstream of the second shock. These flow features are present for all LCOs analysed in this document.

4 STABILITY INVESTIGATIONS

As starting point for the LCO investigations, unstable flow settings should be validated with a classical flutter analysis before starting time-consuming time-domain computations. Since the aerodynamic model is computed with the Pulse method, only unsteady linear aerodynamics are covered. Hence the possibility of so called 'bad flutter' is neglected. This means that no reduction of damping with increased motion amplitude is expected.

The damping results are compared with measured displacement amplitudes, which have been integrated from the available acceleration sensors. As frequency the

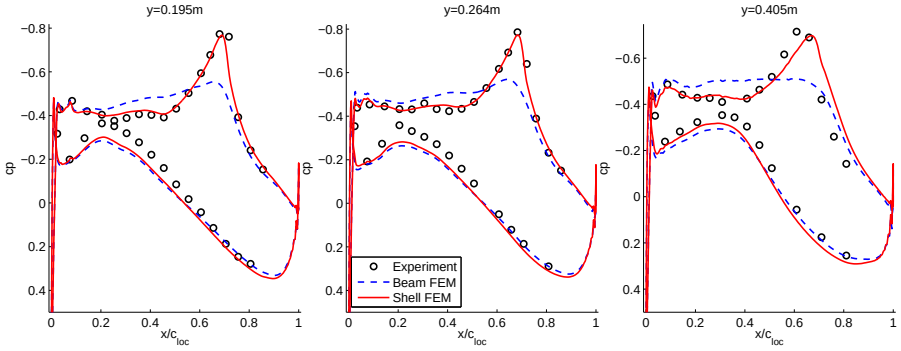

Figure 6: Pressure comparison beam FE-model and shell FE-model results for Mach number Ma = 0.819, Reynolds number Re = $1.33 \cdot 10^6$ and angle of attack $\alpha = 0.0°$

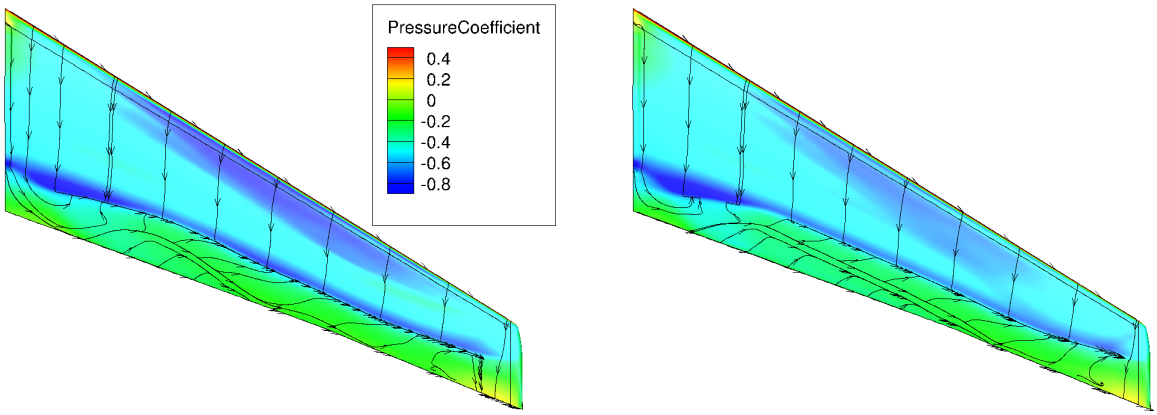

(a) Ma=0.8547 (b) Ma=0.8844

Figure 7: Pressure coefficient and skin-friction lines, two different *Mach*-numbers, Re=$1.69 \cdot 10^6$, $\alpha = 2.7°$

dominating frequency from the acceleration sensor signals is used.

The unsteady Pulse computations use the resulting deformation of a static CFD-CSM computation as boundary condition. For the computation of the steady flow solution a linear and a non-linear structural model is used. The structural input modes for the Pulse computation are also differing. The linear analysis used the eigenmodes of the unloaded structural model, while the non-linear analysis used the modes of an eigenvalue analysis in the non-linear deformed structural condition. The unsteady aerodynamics of different frequencies are then used in the p-k-method to compute the damping ratio D and the reduced frequency $k = 2\pi f c_{ref}/v_{ref}$.

The first investigation is performed for a *Mach*-number range between $Ma = 0.8495$ and $Ma = 0.8844$, but a constant angle of attack $\alpha = 2.69°$ and *Reynolds*-number $Re = 1.69 \cdot 10^6$.

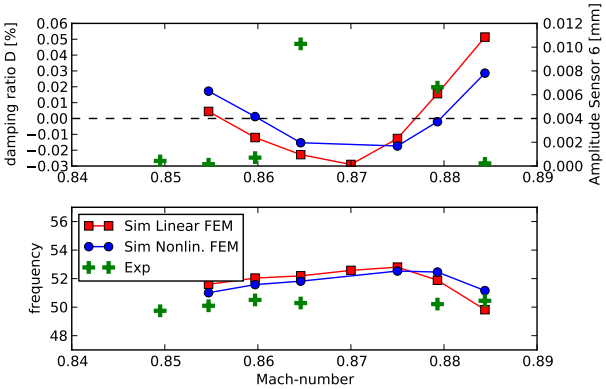

Figure 8: Damping and frequency of p-k-method for *Mach*-number range, compared to acceleration sensor 6 displacement amplitude and dominating frequency from experiment (exp)

Figure 8 shows the results of these two types of simulations. Both methods show an unstable range, but only the unstable range for the non-linear structural model fits perfectly to the measured unstable *Mach*-numbers. The main reason for this behaviour is the difference in the steady flow features. Figure 9 compares the steady pressures for the two methods combined with the airfoil cambering. It can be seen that a small change in cambering leads to noticeable changes in the steady pressures. For comparison reasons steady pressures have also been computed for an aerodynamic surface deformed with the result of a non-linear structural computation which has used the aerodynamic loads of the linear CFD-CSM computation as input. This shows that the CFD-CSM loop itself has no influence on the cambering.

The difference in frequency in Figure 8 between the simulations and the experiment can be explained with around 3Hz difference of the first bending eigenmode between structural model and measured eigenfrequencies from a ground vibration test.

Figure 10 compares the unsteady pressures based on the steady computations with the linear and non-linear FEM to the experiment. Most important in these plots are the differences between the two simulations. They show larger differences especially for the most important outer cut. Also the cut at $y = 4.05m$ shows a slightly better result for the simulation with non-linear FEM.

Figure 11 shows the flutter results for a dynamic-pressure study at constant *Mach*-number. Also here a very good agreement to the experiment can be observed.

So altogether four different unstable experimental points can be used for LCO simulations.

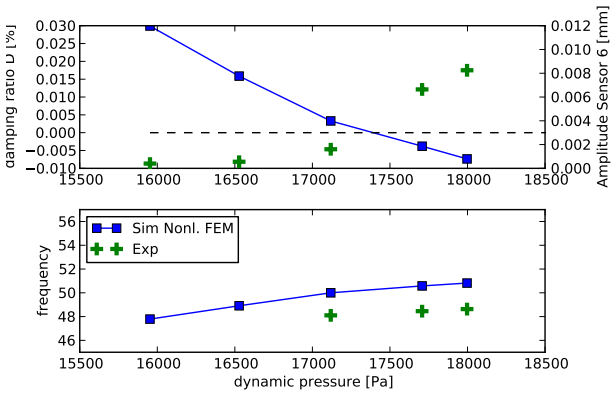

Figure 11: Damping and frequency of p-k-method for dynamic pressure range for constant *Mach*-number, $Ma = 0.8646$, compared to acceleration sensor 6 displacement amplitude and dominating frequency from experiment (exp)

5 LCO ANALYSIS

Section 4 has revealed different flow conditions which allow to perform time-domain flutter simulations. All these simulations reveal limit cycle oscillations. In this paper the focus is set to the LCO with the best agreement to the experiment. This is the LCO for *Mach*-number $Mach = 0.8646$ and dynamic pressure $q = 17.7 \cdot 10^3$ Pa.

Figure 12 shows the displacements of sensor 6 for two time-domain simulation. The simulations have been started with a start disturbance fitting to the experimental values. As one can see, the simulation with dynamic pressure $q = 17.7 \cdot 10^3$Pa has almost not changed its amplitude anymore.

Figure 14 shows mean steady and unsteady pressures for the selected LCO state for the linear, frequency-domain investigation aerodynamics and the LCO aerodynamics. The outer cut shows strong differences in the magnitude. The sharp shock peak from the unsteady linear aerodynamics is flattened due to

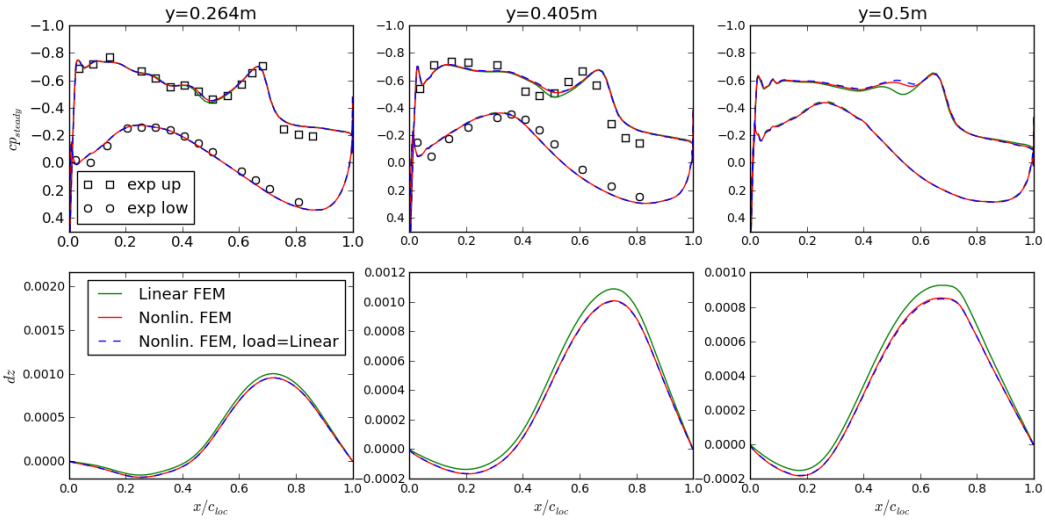

Figure 9: Steady pressures and cambering for $Ma = 0.8793$, $Re = 1.69 \cdot 10^6$ and $\alpha = 2.69°$

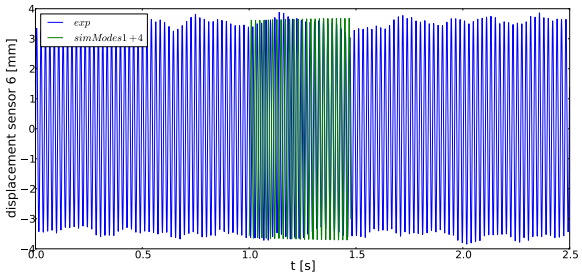

(a) $q = 17.7 \cdot 10^3$ Pa

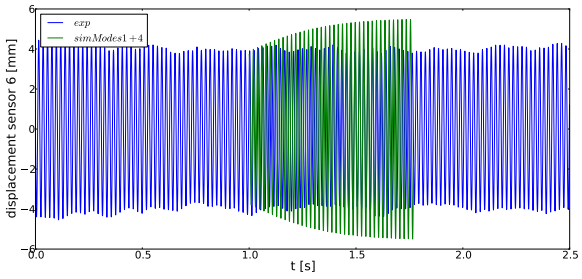

(b) $q = 18.0 \cdot 10^3$ Pa

Figure 12: Displacement of acceleration sensor 6 in simulation and experiment vs. time for $Mach = 0.8646$ and different dynamic pressures q

strong shock movement. Overall a very good agreement to the experiment can be found.

The unsteady work per cycle is shown in Figure 13. The plot compares the aerodynamic work of the linear frequency-domain aerodynamics to the time-domain LCO aerodynamics. This plots shows, that the upstream shock changes its energy input to the wing strongly with increasing amplitude. This reduction of energy input explains the occurrence of limit cycle oscillations and has prevented the windtunnel experiment from a destructive incident.

6 CONCLUSION

This paper showed the high accuracy which can be reached with nowadays simulation methods in the field of transonic aeroelasticity. Therefore the detailed analysis of the AEROSTABIL limit-cycle oscillation experiments by means of high fidelity simulations has been shown. As already seen in previous publications the key to understand this experiment is the detailed structural model, which shows a strong influence of cambering on the transonic aerodynamics. In the LCO region additionally strong separation increases the demanding flow complexity. Nevertheless the simulations allowed to accurately predict the unstable experimental points. This was the requirement to perform limit cycle oscillation simulations. In this connection the measured limit cycle amplitudes can also be discovered in the simulation with a satisfying accuracy. The non-linear mechanism to explain the limit cycles are strong shock movement in

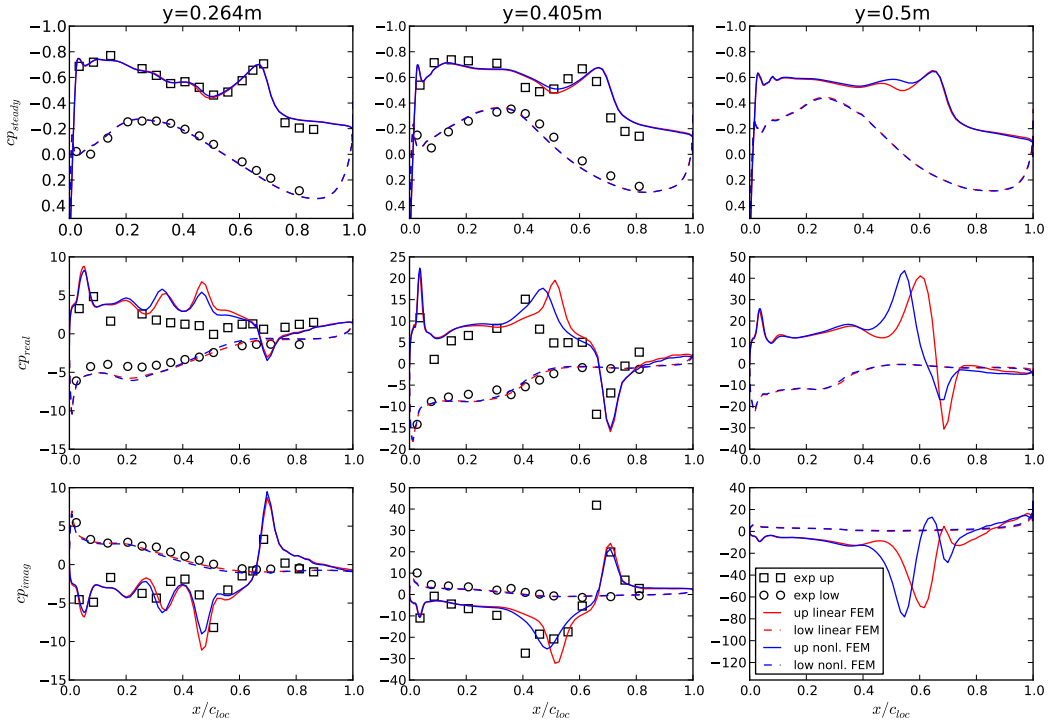

Figure 10: Steady pressures and unsteady pressure transfer-functions displayed in real and imaginary part for $Ma = 0.8793$, non-linear vs. linear steady CFD-CSM solution as input, $Re = 1.69{\cdot}10^6$ and $\alpha = 2.69°$

the outer-wing area.

7 REFERENCES

[1] Klaus-Juergen Bathe and Edward L. Wilson. *Numerical Methods in Finite Element Analysis*. Englewood Cliffs, N. J., Prentice-Hall, 1976.

[2] A. Beckert and H. Wendland. Multivariate interpolation for fluid-structure-interaction problems using radial basis functions. *Aerospace Science and Technology*, 5:125–134, 2001.

[3] G. Dietz, G. Schewe, F. Kiessling, and M. Sinapius. Limit-cycle-oscillation experiments at a transport aircraft wing model. In *International Forum on Aeroelasticity and Structural Dynamics (IFASD), Amsterdam*, 2003.

[4] Richard Dwight. An implicit lu-sgs scheme for finite-volume discretizations of the navier-stokes equations on hybrid grids. DLR-FB-2005-05 ISSN 1434-8454, DLR, 2005.

[5] Thomas Gerhold and Martin Galle. Calculation of complex three-dimensional configurations employing the DLR TAU-code. *AIAA Paper 97-0167*, 1997.

[6] H. J. Hassig. An approximate true damping solution of the flutter equation by determinant iteration. *Journal of Aircraft*, 8(11):885–889, 1971.

[7] Antony Jameson. Time dependent calculations using multigrid, with applications to unsteady flows past airfoils and wings. In *Proc. 10th Comp. Fluid Dyn. Conf., Honolulu, HI, USA, June 24-26, 1991, AIAA-Paper 91-1596*, 1991.

[8] F. R. Menter. Zonal two-equation k-omega turbulence models for aero-

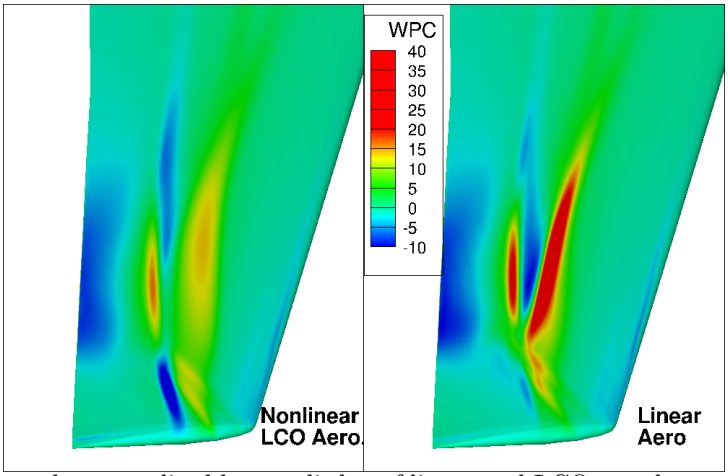

Figure 13: Work per cycle, normalised by amplitdue of linear and LCO aerodynamics ($Mach = 0.8646$, $q = 17.7 \cdot 10^3$Pa, $Re = 1.43 \cdot 10^6$

dynamic flows. *AIAA Journal*, page 2906, 1993.

[9] MSC. *Implicit Nonlinear (SOL 400/600) Users Guide*, 2013. URL: www.mscsoftware.com.

[10] T. C. S. Rendall and C. B. Allen. Parallel efficient mesh motion using radial basis functions with application to multi-bladed rotors. *International Journal for Numerical Methods in Engineering*, (81):89–105, 2010.

[11] W.A. Silva and D. E. Raveh. Development of unsteady aerodynamic state-space models from cfd-based pulse responses. *AIAA/ASME/ASCE/AHS/ASC Structures, Structural Dynamics and Materials Conference and Exhibit*, 42:51–117, 2001.

[12] Bernd Stickan and Johannes Dillinger. Steady and unsteady simulations of aerostabil windtunnel experiments. In *International Forum on Aeroelasticity and Structural Dynamics (IFASD), Paris*, 2011.

[13] Bernd Stickan, Johannes Dillinger, and Gnther Schewe. Limit-cylcle-oscillation simulations of aerostabil windtunnel experiments. In *International Forum on Aeroelasticity and Structural Dynamics (IFASD), Bristol*, 2013.

[14] Bernd Stickan, Johannes Dillinger, and Günter Schewe. Computational aeroelastic investigation of a transonic limit-cycle-oscillation experiment at a transport aircraft wing model. *Journal of Fluids and Structures*, 49(0):223 – 241, 2014.

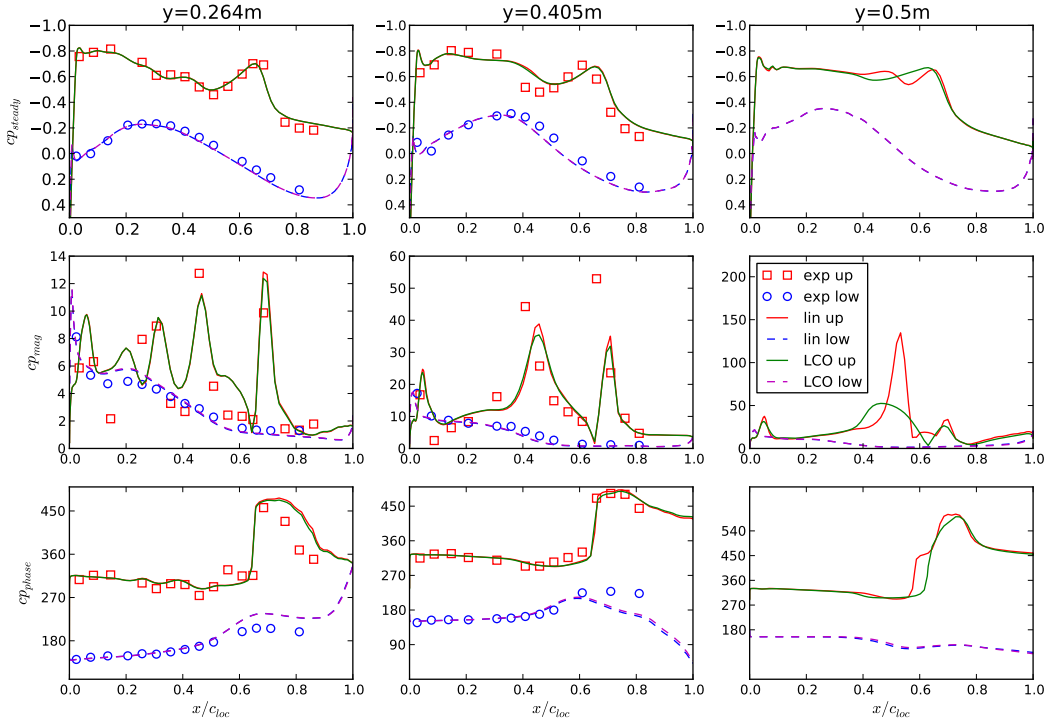

Figure 14: steady and unsteady aerodynamics, $Mach = 0.8646$, $q = 17.7 \cdot 10^3$Pa, $Re = 1.43 \cdot 10^6$

8 COPYRIGHT STATEMENT